

PRODIGE – envelope to disk with NOEMA

VII. (Complex) organic molecules in the NGC1333 IRAS 4B1 outflow: A new laboratory for shock chemistry

L. A. Busch¹,^{*,1} J. E. Pineda¹, P. Caselli¹, D. M. Segura-Cox^{2,1}, S. Narayanan¹, C. Gieser³, M. J. Maureira¹, T.-H. Hsieh^{4,5,1}, Y. Lin¹, M. T. Valdivia-Mena^{6,1}, L. Bouscasse⁷, Th. Henning³, D. Semenov^{8,3}, A. Fuente⁹, Y.-R. Chou¹, L. Mason¹, P. C. Cortés^{10,11}, L. W. Looney¹², I. W. Stephens¹³, M. Tafalla¹⁴, A. Dutrey¹⁵, W. Kwon^{16,17}, and P. Saha⁵

(Affiliations can be found after the references)

Received ; accepted

ABSTRACT

Context. Shock chemistry is an excellent tool to shed light on the formation and destruction mechanisms of complex organic molecules (COMs). The L1157-mm outflow is the only low-mass protostellar outflow that has extensively been studied in this regard.

Aims. We aim to map COM emission and derive the molecular composition of the protostellar outflow driven by the Class 0 protostar NGC 1333 IRAS 4B1 to introduce it as a new laboratory to study the impact of shocks on COM chemistry.

Methods. We used the data taken as part of the PRODIGE (PROtostars & DIsks: Global Evolution) large program to compute integrated intensity maps of outflow emission to identify spatial differences between species. The emission spectra were then analysed towards two positions, one in each outflow lobe, by deriving synthetic spectra and population diagrams assuming conditions of local thermodynamic equilibrium (LTE).

Results. In addition to typical outflow tracers such as SiO and CO, outflow emission is seen from H₂CO, HNCO, and HC₃N, as well as from the COMs CH₃OH, CH₃CN, and CH₃CHO, and even from deuterated species such as DCN, D₂CO, and CH₂DOH. Maps of integrated intensity ratios between CH₃OH and DCN, D₂CO, and CH₃CHO reveal gradients with distance from the protostar. For DCN and D₂CO, this may reflect their prestellar abundance profile, provided the outflow is young enough, while an explanation is still required for CH₃CHO. Intensity ratio maps of HC₃N and CH₃CN with respect to CH₃OH peak in the southern lobe where temperatures are highest. This may point to enhanced HC₃N and CH₃CN formation at this location, potentially in the warmer gas phase. Rotational temperatures are found in the range \sim 50–100 K, which is, on average, warmer than for the L1157-B1 shock spot (\lesssim 30 K). Abundances with respect to CH₃OH are higher by factors of a few than for L1157-B1.

Conclusions. For the first time, we securely detected COMs CH₃CN, CH₃CHO, and CH₂DOH in the IRAS 4B1 outflow, serendipitously with limited sensitivity and bandwidth. Targeted observations will enable the discovery of new COMs and a more detailed analysis of their emission. Morphological differences between molecules in the IRAS 4B1 outflow lobes and their relative abundances provide first proof that this outflow is a promising new laboratory for shock chemistry, which will offer crucial information on COM formation and destruction as well as outflow structure and kinematics.

Key words. Astrochemistry – ISM: molecules – ISM: jets and outflows – Stars: formation – Stars: protostars – Stars: low-mass

1. Introduction

One of the key questions in astrochemistry is to understand the growth of molecular complexity during the process of star formation, including the formation and destruction processes of complex organic molecules (COMs; \geq 6 atoms and carbon-bearing; [Herbst & van Dishoeck 2009](#)). In general, COMs can either form in the gas phase or in the solid phase on icy dust grain surfaces, from which they can desorb through numerous thermal and non-thermal processes (e.g. see review on COM chemistry by [Ceccarelli et al. 2023](#)). To shed light on COM formation and destruction, observing sites of shock chemistry have become increasingly popular. Shock waves passing through quiescent medium greatly impact the local chemical composition (e.g. [Draine 1995](#)). They compress and temporally heat the medium, for example, enabling endothermic reactions to take place in the gas phase and sublimating ice mantles, thereby, releasing molecules to the gas phase. Stronger shocks may even sputter or completely destroy grains (e.g. [Lenzuni et al. 1995](#);

[Jiménez-Serra et al. 2008](#); [Gusdorf et al. 2008](#)). These processes happen on a rather short timescale (100s to 1000s of years; e.g. [Burkhardt et al. 2019](#)), adding time constraints to the molecular compositions.

Sites of shock chemistry include protostellar outflows that interact with the ambient medium. The outflow driven by the Class 0 protostar L1157-mm (L1157 hereafter) has been the target of numerous projects, in which the source presented itself as a perfect laboratory to study COM chemistry ([Bachiller & Pérez Gutiérrez 1997](#)). Single-dish and interferometric studies that reported detections of (complex) organic molecules in this source include, for example, [Arce et al. \(2008](#), HCOOH, CH₃OCHO, CH₃CN), [Codella et al. \(2009](#), CH₃CN), [Sugimura et al. \(2011](#), HCOOH, CH₃OCHO, CH₃CHO), [Mendoza et al. \(2014](#), HNCO, HCNO, NH₂CHO), [Fontani et al. \(2014](#), HDCO, CH₂DOH), [Lefloch et al. \(2017](#), HCOOH, H₂CCO, CH₃OCH₃, HCOCH₂OH, C₂H₅OH), [Mendoza et al. \(2018](#), HC₃N, HC₅N), and [Codella et al. \(2020](#), CH₃OH, CH₃CHO). Several of these studies concluded that COMs can be as abundant or even more abundant in shocked regions than in hot corinos (e.g. [Arce et al. 2008](#); [Mendoza et al. 2014](#); [Lefloch et al. 2017](#)) or shocked

* 1busch@mpe.mpg.de

molecular clouds located in the Galactic centre (Arce et al. 2008), such as G0.693+0.027 (e.g. see Fig. 11 in Busch et al. 2024). In addition, spatial variations of COM emission provided insights into the likely dominating formation pathways. For example, NH_2CHO emission peaks farther away from the protostar in the outflow than CH_3CHO (Codella et al. 2017; López-Sepulcre et al. 2024), which has been interpreted as NH_2CHO being formed later than CH_3CHO . Based on astrochemical models, the authors concluded that NH_2CHO is dominantly formed in the post-shock gas phase, while CH_3CHO could be formed in the gas phase directly or desorbed from dust grain surfaces. With the knowledge gained from this template outflow, the search for other outflows is well underway. Complex organic molecules other than CH_3OH have been mapped towards the outflow system driven by the NGC1333 IRAS 4A protostellar, which revealed emission from CH_3CHO , CH_3OCH_3 , and NH_2CHO (De Simone et al. 2020), and towards the HOPS 409 outflow located in the OMC-2/3 filament (CH_3CN ; Bouvier et al. 2025).

In this article, we present another young protostellar outflow and discuss its potential as new laboratory for shock chemistry. The outflow driven by the Class 0 protostar NGC1333 IRAS 4B1, which forms a binary system with IRAS 4B2 (2450 au separation; Tobin et al. 2016), has been mapped in emission of various molecules, such as HCN (Choi 2001), H_2O (Desmurs et al. 2009), H_2CO (Di Francesco et al. 2001), H_2S and OCS (Miranzo-Pastor et al. 2025), as well as CO, SiO , and SO (Jørgensen et al. 2007; Stephens et al. 2018; Podio et al. 2021) but COMs, other than CH_3OH (Jørgensen et al. 2007; Sakai et al. 2012), remained undetected. Additionally, *Herschel*-PACS spectra towards the southern lobe revealed one of the richest far-infrared spectra amongst young low-mass protostellar sources with numerous highly excited H_2O , OH, CO emission lines (Herczeg et al. 2012). Following-up on this, the outflow has also been observed by the James Webb space telescope (JWST) as part of the JWST Observations of Young protoStars (JOYS; van Dishoeck et al. 2025; Francis et al. 2025). The southern lobe was mapped in emission of $\text{H}_2\text{S}(1)$, $[\text{Fe II}]^4F_{7/2} - ^4F_{9/2}$, and the CO_2 15 μm band. Additional spectra show intense emission from hot C_2H_2 (600 K) and HCN. We report first detections of the following COMs towards the IRAS 4B1 outflow: CH_3CN , CH_3CHO , and deuterated methanol (CH_2DOH). We identify spatial variations in the outflow emission and derive abundances that provide insights into the outflow structure and kinematics as well as the impact of shocks on the chemical composition.

2. Observations

2.1. PRODIGE

The IRAS 4B binary system was observed as part of the PROtostars & DISks: Global Evolution (PRODIGE, PIs: P. Caselli and Th. Henning) large program. PRODIGE is a MPG/IRAM Observatory Program (MIOP, Project ID L19MB) and targeted 30 Class 0/I protostellar systems in the Perseus molecular cloud ($D = 294 \pm 17$ pc; Zucker et al. 2019) with the Northern Extended Millimetre Array (NOEMA) at 1 mm.

The data were taken with the Band 3 receiver and using the PolyFix correlator tuned to a local-oscillator (LO) frequency of 226.5 GHz. This setup covers a total bandwidth of 16 GHz with a channel width of 2 MHz ($\sim 2.6 \text{ km s}^{-1}$), divided into four sidebands: lower outer (214.7–218.8 GHz), lower inner (218.8–222.8 GHz), upper inner (230.2–234.2 GHz), and upper outer (234.2–238.3 GHz). Additional 39 windows at high spectral-resolution (62.5 kHz or $\sim 0.09 \text{ km s}^{-1}$ channel width), each cov-

ering a 64 MHz bandwidth, were placed within the 16 GHz bandwidth. The observations probe spatial scales of approximately 300 au (corresponding to the highest angular resolution of $\sim 1''$) to 5000 au at the distance of Perseus. The phase centre is at $(\alpha, \delta)_{\text{J2000}} = (03^{\text{h}}29^{\text{m}}12\text{:}02, 31^{\circ}13'08\text{''}03)$. The PRODIGE observations of IRAS 4B were conducted in January and April 2022 in array configurations C and D, covering baselines from 24 m to 400 m.

For the data calibration of the PRODIGE data we used the standard observatory pipeline within GILDAS/CLIC¹ package. Continuum subtraction and data imaging were performed with the GILDAS/MAPPING package using the `uv_baseline` and `clean` tasks, respectively. For the imaging of the continuum maps we used `robust = 1`, to improve the angular resolution, and for the spectral line cubes we used natural weighting to minimise noise. More details on data reduction and imaging can be found in Gieser et al. (2024).

Integrated intensity maps were created using the high spectral-resolution data for selected molecules except for CO and HNCO (see Sect. 3.1). Table A.1 summarises all transitions used for the various maps with their spectroscopic information. The average noise in these cubes is about 10 mJy beam $^{-1}$ (62.5 kHz channel width). For the spectral-line analysis, spectra were extracted towards two selected positions from the low spectral-resolution (2 MHz) cubes, as more molecular lines are covered (see Sect. 3.3). These have noise levels of about 2 mJy beam $^{-1}$.

2.2. ALPPS

Additionally, we made use of data taken with the Atacama Large Millimetre Array (ALMA) as part of the ALMA Perseus Polarization Survey (ALPPS; Cortes et al. 2025) towards IRAS 4B1 at an angular resolution of $0.37'' \times 0.30''$ ($PA = -20.6^\circ$). The spectral setup covers a bandwidth of 1.9 GHz from 335.5 GHz to 337.4 GHz at 0.976 MHz spectral resolution ($\sim 0.9 \text{ km s}^{-1}$). The noise level measured in the cube is 22 mJy beam $^{-1}$. We use the data to produce maps of the outflow emission at high angular resolution. Additional transitions of molecules analysed with the PRODIGE data are added to the temperature and column density determinations. To combine both data sets, we needed to smooth the ALPPS data to the angular ($1.1'' \times 0.8''$) and 2 MHz spectral resolution of the PRODIGE data using the `convolve_to` python command and the `resample` command in CLASS, respectively.

3. Results

First, we study the outflow emission morphology of the detected molecules in Sect. 3.1 and highlight differences based on maps showing ratios of integrated intensities with respect to CH_3OH in Sect. 3.2. Molecular rotational temperatures and column densities are derived in Sect. 3.3 towards two positions, one in each outflow lobe, and assuming local thermodynamic equilibrium (LTE). The derived molecular composition is subsequently compared to the one in L1157-B1 in Sect. 4.

3.1. Emission morphology

Figure 1 shows integrated intensity maps towards IRAS 4B1 of SiO 2–1 (colour-scales), CH_3OH 4₂ – 3₁, and DCN 3–2 (contours), separated in red- and blueshifted emission (with respect to the systemic velocity $v_{\text{sys}} = 6.8 \text{ km s}^{-1}$; Busch et al. 2025).

¹ <https://www.iram.fr/IRAMFR/GILDAS/>

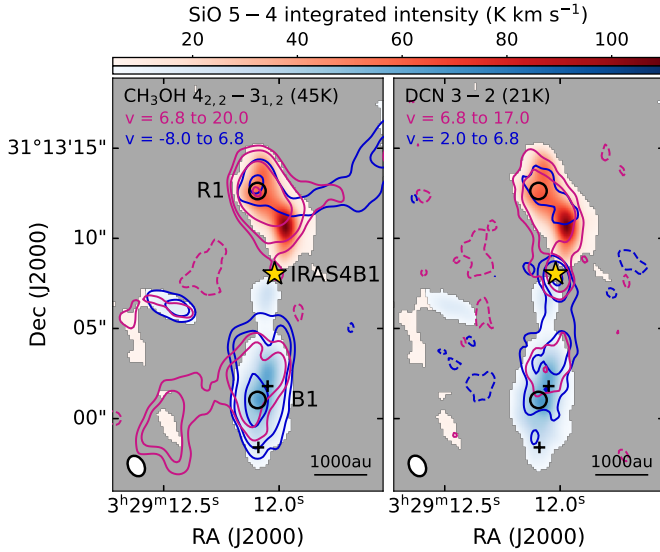


Fig. 1. Integrated intensity maps towards IRAS 4B1 (yellow star) for SiO 2–1 ($E_u = 31$ K; colour) and CH₃OH 4₂–3₁ and DCN 3–2 ($E_u = 45$ K and 21 K, respectively; contours). The SiO maps are integrated from -25 to 6 km s $^{-1}$ and 6.8 to 47 km s $^{-1}$ and show emission above 10σ with $\sigma_{\text{blue}} = 0.42$ K km s $^{-1}$ and $\sigma_{\text{red}} = 0.49$ K km s $^{-1}$. Contours are at $-30\sigma, -15\sigma, 15\sigma, 30\sigma$, and then increase by a factor of 3 for CH₃OH ($\sigma_{\text{blue}} = 0.25$ K km s $^{-1}$ and $\sigma_{\text{red}} = 0.23$ K km s $^{-1}$) and at $-10\sigma, -5\sigma, 5\sigma, 10\sigma$, and then increase by a factor of 3 for DCN ($\sigma_{\text{blue}} = 0.17$ K km s $^{-1}$ and $\sigma_{\text{red}} = 0.24$ K km s $^{-1}$). Velocity ranges (in km s $^{-1}$) used for the integration of CH₃OH and DCN emission are indicated in the top left. The HPBW is shown in the bottom left. Positions R1 and B1 were selected for further spectral-line analysis (Sect. 3.3). Black crosses indicate H₂ knots (Choi & Lee 2011).

The emission extends to the north and south from the central protostar and can be associated with the outflow driven by that protostar. Red- and blueshifted emission at velocities of $\Delta v = |v_{\text{sys}} - v| < 10$ km s $^{-1}$ is present in both lobes, suggesting that the outflow lies close to the plane of the sky. The overlap of red- and blueshifted emission is also observed for SiO (cf. Figs. A.1 and A.2), however, in Fig. 1, we only show emission above 10σ to focus on the dominant SiO features in each lobe. Emission from CH₃OH and DCN spatially coincides with SiO for the most part. Blueshifted SiO emission close to the protostar in the southern lobe and a peak in redshifted SiO emission at $\sim(0'', 2.5'')$ are not evident in CH₃OH emission, while DCN does not extend as far as SiO and CH₃OH in the southern lobe. In addition, CH₃OH reveals arc-like emission features that seem to start from within the main outflow lobes in the north and south and continue NW and SE, respectively. While the NW extension contains red- and blueshifted emission, the SE extension only appears in redshifted emission in our data. These features were proposed to be a second outflow, based on larger-scale methanol maps, which extend beyond our field of view (Sakai et al. 2012). The authors discussed the possibility of IRAS 4B1 consisting of two protostars, each driving an outflow. However, the presence of a second source within IRAS 4B1 remains debated. At spatial scales of $\lesssim 30$ au, continuum maps at 8 mm show no clear evidence for a companion (see Fig. 34 in Segura-Cox et al. 2018), although there is extended fainter emission in addition to the peak. Emission to the east in Fig. 1 originates from the outflow driven by the companion IRAS 4B2 (see also Figs. A.2 and A.3) that is not discussed here further. Low-excitation molecular transitions observed in the 3 mm window reveal an overall complex kinematic

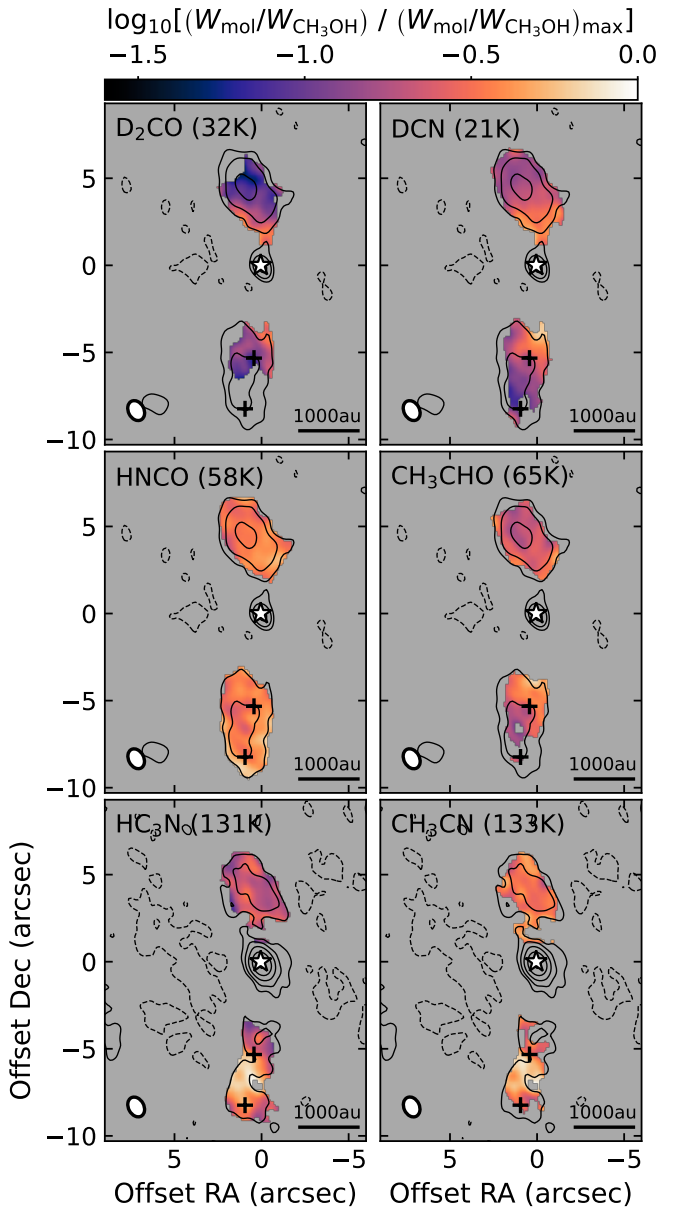


Fig. 2. Integrated intensity ratios, $(W_{\text{mol}}/W_{\text{CH}_3\text{OH}}) / (W_{\text{mol}}/W_{\text{CH}_3\text{OH}})_{\text{max}}$ of various molecular transitions with either CH₃OH 10_{2,9}–9_{3,6} ($E_u = 165$ K; for HC₃N and CH₃CN) or 5_{1,4}–4_{2,2} ($E_u = 56$ K; for D₂CO, DCN, HNCO, and CH₃CHO) towards the IRAS 4B1 outflow. Integrated intensities contain the sum of blue- and redshifted emission (cf. Fig. A.3 and spectra in Fig. A.1). The ratio is only shown if both molecules are above a 5σ threshold, where σ is the noise level in the respective map. Another mask with a $1''$ radius around the protostar is applied to the ratios. Black contours show the integrated intensities of CH₃OH, starting at $-5\sigma, 5\sigma$, and then increasing by a factor of 2, where $\sigma = 0.34$ K km s $^{-1}$. The molecule as well as the upper-level energy of the shown transition are in the top left corner. In all panels, the white star marks the position of IRAS 4B1. The HPBW is shown in the bottom left corner and black crosses mark H₂ knots (Choi & Lee 2011). Spectroscopic information on the shown transitions are given in Table A.1.

structure, which will be studied in detail in a forthcoming paper. Such structures include, for example, the arcs identified here and a streamer candidate (Valdivia-Mena et al. 2024).

Figure A.2 shows additional channel maps of the typical outflow tracers SiO and CO, where intensities were integrated over

10 km s⁻¹ intervals to study substructure at different velocities. At high blueshifted (−30 to −5 km s⁻¹) and redshifted (20 to 45 km s⁻¹) velocities, the emission of the IRAS 4B1 outflow is confined within the southern and northern lobes, respectively, in contrast to the broader lower-velocity emission. This can result from the fact that this higher-velocity component is more inclined or more collimated than the lower-velocity component. The high-velocity emission can likely be associated with a jet component (see also Podio et al. 2021). The presence of various intensity peaks or knots along both lobes may additionally indicate episodic ejection (e.g. Bachiller 1996).

Figure A.3 shows integrated intensity maps of blue- and redshifted emission again for CH₃OH and DCN, and for seven additional organic (i.e. C-bearing) molecules. Example spectra towards positions R1 and B1 (see Fig. 1) are shown in Fig. A.1. Emission from H₂CO and CH₃OH in Fig. A.3 is the most prominent in the outflow. Molecules such as CH₃CHO, DCN, HC₃N, CH₃CN, HNCO, and D₂CO show weaker emission. For HC₃N and CH₃CN, but maybe also HNCO and CH₃CHO, this could be an excitation effect, since the PRODIGE data only cover transitions with higher upper-level energies. Weak (signal-to-noise, S/N ∼ 5), compact emission from *c*-C₃H₂ is detected very close to the protostar. Besides CH₃OH, H₂CO and CO reveal the additional arc-like emission features (Figs. A.2 and A.3). There are extended features of negative intensity for, in particular, CO and H₂CO, which point to missing flux in the PRODIGE data due to missing short spacings (see also Gieser et al. 2025).

3.2. Spatial differences with respect to CH₃OH

To see whether there are morphological differences, we compare all molecules with CH₃OH by deriving ratio maps of integrated intensity, W , that is $R = W_{\text{mol}}/W_{\text{CH}_3\text{OH}}$, and show them normalised by the maximum value, R/R_{max} , in Fig. 2. We only plot pixels, where both integrated intensity values are above a 5σ threshold, where σ is the noise measured in the respective map. The integration intervals differ between molecules (same intervals as in Figs. A.1 and A.3). If we used the same (largest) interval, we would integrate over too much noise leading to more discarded pixels for the weakest transitions. In addition, we apply a mask of a 1'' radius around the protostar because line blending is more severe in the hot corino and might bias the integrated intensity ratios. Because upper-level energies differ between the molecular transitions, meaning that they may probe different excitation conditions, we used two methanol transitions: 10₂ − 9₃ ($E_u = 165$ K) with HC₃N and CH₃CN ($E_u \approx 130$ K) and 5₁ − 4₂ ($E_u = 56$ K) with the other molecules ($E_u = 20$ –65 K), to reduce excitation effects. Additional information on the used transitions are summarised in Table A.1. There is a clear decrease in D₂CO and DCN intensities relative to CH₃OH with increasing distance from the protostar in both lobes by a factor of ∼10. In the southern lobe, a similar but less distinct gradient is seen for CH₃CHO. For HC₃N and CH₃CN, the integrated intensity ratio peaks in between the two H₂ knots (Choi & Lee 2011) in the southern lobe. These trends may still (partially) be a consequence of different excitation conditions but may also probe different chemical processes. This is discussed further in Sect. 4.

3.3. Spectral-line analysis & results

For the spectral-line analysis, we extracted beam-averaged spectra towards one position in the southern lobe (B1) and one in the northern lobe (R1) at (03^h29^m12^s09, 31°13'12".63) and

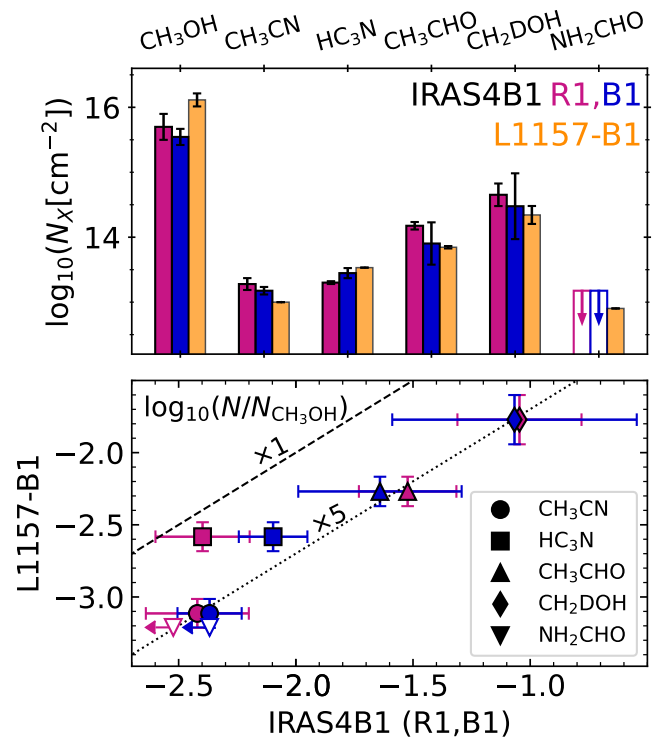


Fig. 3. Column densities (top) and abundances with respect to CH₃OH (bottom) towards B1 and R1 in IRAS 4B1 derived in this work and values obtained for L1157-B1 (see Table A.2). The dashed and dotted black lines indicate equal abundances and a difference of a factor of 5, respectively. Empty bars or symbols with arrows indicate upper limits.

(03^h29^m12^s09, 31°13'12".63), respectively, which correspond to the CH₃OH emission peaks (Fig. 1). We follow the analysis strategy of Busch et al. (2025), where we already derived rotational temperatures and column densities for CH₃OH and CH₃CN isotopologues towards the hot corino IRAS 4B1 amongst other sources. Accordingly, we use the radiative transfer code Weeds, which is an extension of the GILDAS/CLASS software (Maret et al. 2011), and derive population diagrams (PDs; Goldsmith & Langer 1999). Both methods assume local thermodynamic equilibrium (LTE). We refer to Busch et al. (2025) for details; in short: Weeds computes synthetic spectra based on five input parameters, which are column density, rotational temperature, source size, velocity offset from v_{sys} , and line width (i.e. full width half maximum). We assume that the emission is spatially resolved (i.e. beam filling factor = 1). Line widths and velocity offsets can be derived from fitting 1D Gaussian profiles to the spectral lines, using the CLASS command `minimize`, where we fitted one velocity component per molecule.

The best-fit column densities and rotational temperatures are verified with values from PDs, which are shown in Fig. A.4. The PDs were derived for CH₃OH, CH₃CHO, CH₃CN, HC₃N, CH₂DOH, and D₂CO, since they are the only molecules with at least three detected transitions. The temperatures and column densities derived with Weeds and the PDs are summarised in Table A.2 together with the other Weeds parameters. Results from Weeds and the PDs agree widely within the 1σ error bars. Some scatter between the observed data points is evident (e.g. D₂CO in B1). We discussed several reasons leading to such scatter when analysing the PRODIGE data in Busch et al. (2025). Weeds estimates line optical depths based on the input parameters, yielding optically thin lines in all cases. In some PDs, when the linear fit

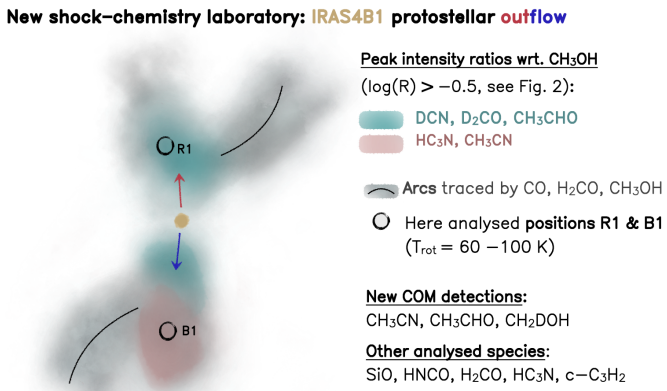


Fig. 4. Cartoon highlighting the main molecular features of the IRAS 4B1 outflow analysed in this work. The main emission morphology of our reference molecule, CH_3OH , is outlined in grey, including the main outflow lobes (red and blue arrows) and additional arc-like features (black lines) of currently unknown origin. Peaks of intensity ratios with respect to CH_3OH are highlighted in teal and pink, depending on the species (cf. Fig. 2). A spectral-line analysis was done towards positions R1 and B1 that yielded rotational temperatures of $T_{\text{rot}} = 60–100$ K (Sect. 3.3). The position of the protostar is indicated in yellow.

was unreliable, we fixed the rotational temperature to get an estimate on the column density. Rotational temperatures range from 50 K to 100 K without significant differences between positions B1 and R1. Column densities derived towards B1 and R1 agree within a factor of 2 and are shown in Fig. 3. They are discussed in a direct comparison with values derived towards the L1157 outflow in Sect. 4.2.

4. Discussion: A new shock-chemistry laboratory

Figure 4 summarises the main molecular features of the IRAS 4B1 outflow derived in this work, including the morphological differences of molecules with respect to CH_3OH , which are further discussed in Sects. 4.1.1 and 4.1.2. In addition, we looked at the morphology at higher angular resolution using ALPPS data (Sect. 4.1.3). In Sect. 4.2 we compare our results with the ones obtained for the L1157 outflow.

4.1. Implications from the morphology

Differences in the emission morphology between molecules can probe different physical conditions but may also be explained by certain chemical processes. In Fig. 2 we mapped the outflow emission from different species in comparison with CH_3OH . Figure 4 highlights the main findings. Since CH_3OH is known to be formed on dust-grain surfaces and is released into the gas phase due to the shocks, it is a suitable reference molecule to interpret any morphological differences with other molecules.

4.1.1. Deuterated species

The intensity ratios for the deuterated species DCN and D_2CO with CH_3OH (Fig. 2 and 4) show a pronounced decrease with increasing distance from the protostar in both lobes. Recently, D_2CO emission was studied towards the IRAS 4A outflows (Chahine et al. 2024), where it shows a similar trend. During the prestellar stage, D_2CO is more efficiently formed on dust-grain surfaces the lower temperatures are, that is closer to the

centre of the prestellar core. Later, upon interaction with the outflow, D_2CO is then released from the grain surfaces. Therefore, the observed gradient along the outflow lobes may reflect the abundance profile that was built up during the prestellar phase, provided the molecules were recently released from grains and gas-phase chemistry has not altered the abundance distribution yet (see also Podio et al. 2024). Whether this also applies to DCN is not entirely clear. Based on a study of DCN towards the L1157 outflow, Busquet et al. (2017) argue that the molecule is a product of both gas- and solid-phase chemistry. Moreover, it is not clear whether DCN or HCN freeze-out as efficiently during the prestellar phase. It was shown in prestellar cores that HCN remains in the gas phase where CO is already frozen-out (e.g. Hily-Blant et al. 2010; Spezzano et al. 2022). These single-dish studies probed larger spatial scales, meaning that freeze-out of DCN and HCN at smaller scales is not excluded when probed with interferometers. Model predictions are also inconclusive as they are heavily dependent on the underlying physical setup (priv. comm.).

4.1.2. CH_3CHO , HC_3N , and CH_3CN

In the southern outflow lobe of IRAS 4B1, we observed decreasing CH_3CHO intensity ratios relative to CH_3OH (Fig. 2) with increasing distance from the protostar, while emission from both COMs is more similar in the northern lobe. In L1157-B1, CH_3CHO and CH_3OH coincide spatially (Codella et al. 2020), implying that CH_3CHO is also formed in the solid phase or, as proposed by Codella et al. (2017, 2020), rapidly in the gas phase as soon as the reactants arrive in the gas phase from the grains. The gradient that we observe may suggest that abundances drop faster for CH_3CHO than for CH_3OH starting from IRAS 4B1. In contrast to CH_3OH , CH_3CHO can also efficiently form in high-temperature gas (e.g. Garrod et al. 2022). Therefore, to see whether the observed emission gradient coincides with a temperature gradient, we derived maps of rotational temperature using two transitions with different upper-level energies and assuming LTE and that the transitions trace the same gas. The maps for HC_3N and CH_3OH are shown in Fig. 5 and reveal temperatures from 30–100 K with HC_3N probing overall slightly higher temperatures. However, the general trends are similar for both molecules: in the northern lobe, temperature increases from east to west within the northern lobe. In the southern lobe, temperature increases with increasing distance from the protostar, peaks in between the two H_2 knots, and decreases again at the tip of the lobe. The observed emission gradient between CH_3CHO and CH_3OH is thus anticorrelated with the temperature gradient in the southern lobe. It is not clear to us, what this may infer. Instead of temperature, other parameters, such as density variations or cosmic rays (Pineda et al. 2024) may play a more dominating role.

The intensity ratios for HC_3N and CH_3CN (Fig. 2 and 4) follow the temperature map, more in the southern than the northern lobe, suggesting that their abundances are enhanced in the higher temperature gas. Gas-phase formation was also proposed for CH_3CN and HC_3N in the L1157 outflow (Codella et al. 2009; Mendoza et al. 2018). For CH_3CN , this may also be supported by the fact that the column density ratio between CH_3OH and CH_3CN , which is ~ 0.005 towards the IRAS 4B1 outflow, is a factor of 2 smaller than the one derived towards the central hot corino (Busch et al. 2025), where even higher temperatures can facilitate gas-phase formation of CH_3CN (Giani et al. 2023). In addition, JWST spectra revealed rich spectra including features from HCN and C_2H_2 (van Dishoeck et al. 2025) that may be in-

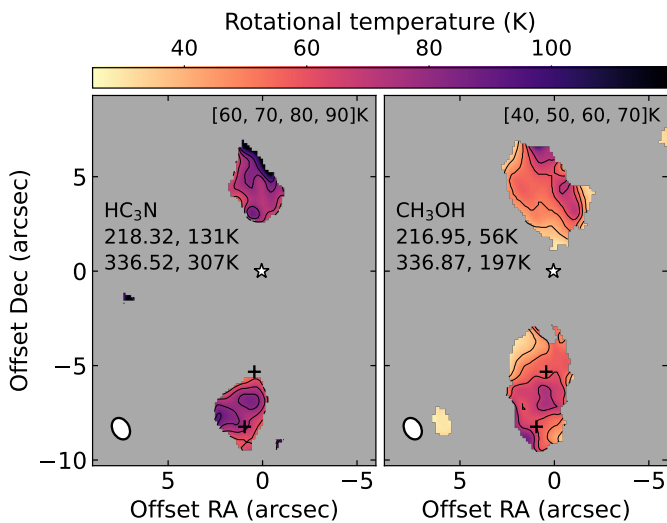


Fig. 5. Rotational temperatures derived from two transitions of HC_3N and CH_3OH assuming LTE. Rest frequencies (in GHz) and upper-level energies of the transitions are written below the molecules. Contour levels are shown in the top right. Markers are the same as in Fig. 2. The HPBW is shown in the bottom left corner.

volved in the enhanced production of HC_3N and CH_3CN (e.g. Taniguchi et al. 2019).

4.1.3. Implications from ALPPS data

Observations of the L1157 outflow at high angular resolution revealed that the L1157-B1 shock spot in the blueshifted lobe consists of several smaller clumps, whose molecular compositions and physical conditions differ (Benedettini et al. 2007, 2013; Codella et al. 2009, 2020), offering insights into the outflow structure, kinematics, and chemistry. Using ALPPS data, we show integrated intensity maps of CH_3OH $7_{1,7}-6_{1,6}$ (the only bright COM covered in that survey) and C^{34}S $7-6$ in Fig. A.2. Similar to L1157-B1, these observations at $\sim 3\times$ higher angular resolution than PRODIGE reveal a highly structured outflow morphology with several intensity peaks. In addition, the morphology of the CH_3OH emission in the southern lobe resembles a bow-shock, while the C^{34}S emission forms a weak S-shape, which is indicative of jet precession (e.g. Bachiller et al. 2001). Therefore, future observations of more species at higher angular resolution will provide deeper insight into the outflow's kinematics and chemistry.

4.2. Comparison with L1157-B1

We compare the column densities and abundances with respect to CH_3OH that we derived towards positions IRAS 4B1-B1 and R1 with literature values from L1157-B1, which were derived in interferometric observations, in Fig. 3 (see Table A.2). Overall, column densities agree within a factor of 2 between the sources, while abundances with respect to CH_3OH are higher towards R1 and B1 in IRAS 4B1. Most abundances differ by a factor 5, suggesting that the chemistry may essentially be the same. One of the reasons for the difference of a factor 5 may be an underestimation of optical depth, hence column density of CH_3OH , which is quite abundant in the outflow. The overall similar chemical composition is interesting given that both outflow showcase different physical conditions. We derived the molecu-

lar composition at positions that are much closer to IRAS 4B1 ($D \sim 1500 - 2000$ au) than L1157-B1 is to its protostar ($D \sim 30\,000$ au; Arce et al. 2008). Related to that, rotational temperatures that we derived, for example, for CH_3OH and CH_3CHO (60–80 K) are significantly higher than towards L1157-B1 but also the IRAS 4A outflow ($\sim 10-20$ K; De Simone et al. 2020; Codella et al. 2020). On the other hand, rotational temperatures derived from CH_3CN in L1157-B1 range from 50 K to 130 K (Codella et al. 2009), similar to what we derived for this molecule. Generally, higher temperatures suggest that volume densities are higher, which may hint at stronger shocks (McKee & Hollenbach 1980). Moreover, the observed subthermal excitation of H_2O at 1500 K observed in *Herschel*-PACS spectra in the southern lobe requires a density of the order of 10^6 cm^{-3} (Herczeg et al. 2012), which makes the IRAS 4B1 outflow a site of a high (pre-)shock density (see also van Dishoeck et al. 2025).

The different maximum spatial extent also implies different outflow ages or shock timescales. The compact IRAS 4B1 outflow was proposed to be very young (a few 100 yr; Choi 2001; Yıldız et al. 2015), and is, therefore, younger than the L1157 outflow (a few 1000 yr; e.g. Yıldız et al. 2015; Kwon et al. 2015; Podio et al. 2016). The timescale associated with the age of the IRAS 4B1 outflow could be crucial for post-shock gas-phase chemistry. For example, a period of $\lesssim 1000$ yr is associated with the delayed formation of NH_2CHO compared with CH_3CHO in L1157-B1, which was mentioned in the introduction (Sect. 1; Codella et al. 2017). We do not detect NH_2CHO . If it remains undetected in more sensitive future observations towards the outflow of IRAS 4B1, this may suggest that the chemistry in the post-shock gas is in an early phase, meaning that a significant amount of NH_2CHO has not yet formed. Therefore, the young age of the IRAS 4B1 outflow may be the perfect test bed to study grain-surface versus gas-phase formation of COMs.

5. Summary

We used data taken as part of the PRODIGE large program and ALPPS to study the emission of organic molecules, including COMs, towards the outflow driven by the Class 0 protostar NGC1333 IRAS 4B1. We posit the potential of this outflow to be a new laboratory for the study of COMs in shocked media. Our main findings are the following:

- We report the first detection of the COMs CH_3CN , CH_3CHO , and deuterated methanol (CH_2DOH) towards this outflow.
- We investigated the morphology of the outflow emission of these three COMs, CH_3OH , and simpler species (HC_3N , HNC , CO , DCN , D_2CO , H_2CO , $c\text{-C}_3\text{H}_2$). The deuterated species DCN and D_2CO showed a gradient with respect to CH_3OH , where they would peak closer to the protostar. This likely reflects the DCN and D_2CO abundance profiles from the prestellar phase. Acetaldehyde (CH_3CHO) showed a similar gradient in the southern lobe, which still needs an explanation. In the southern lobe, intensity ratios of HC_3N and CH_3CN with respect to CH_3OH followed the temperature variations, suggesting that the N-bearing molecules are (additionally) formed in the hotter post-shock gas phase.
- Methanol emission at high angular resolution using ALPPS data, reveal a highly structured outflow morphology, which is also seen in L1157-B1.
- Towards one position in the northern lobe (R1) and one in the southern lobe (B1), we derived on average higher rotational temperatures (50–100 K) and higher abundances with

respect to CH₃OH by factors of a few than towards L1157-B1.

Future observations at higher angular resolution that are as sensitive as those towards L1157-B1 will enable us to detect less abundant COMs and build a comprehensive chemical inventory of the IRAS 4B1 outflow, which we can compare to the one of the central hot corino. Together with modelling efforts, this will deliver crucial information on COM formation and destruction processes as well as outflow structure and kinematics.

Acknowledgements. The authors thank the IRAM staff at the NOEMA observatory for their support in the observations and data calibration. This work is based on observations carried out under project number L19MB with the IRAM NOEMA Interferometer. IRAM is supported by INSU/CNRS (France), MPG (Germany) and IGN (Spain). L.A.B, J.E.P., P.C., M.J.M., C.G., Y.L., D.S., Y.C., L.M., S.N. acknowledge the support by the Max Planck Society. D.S. was funded by the Deutsche Forschungsgemeinschaft (DFG, German Research Foundation) – project number: 550639632. This project is co-funded by the European Union (ERC, SUL4LIFE, grant agreement No101096293). A.F. also thanks project PID2022-137980NB-I00 funded by the Spanish Ministry of Science and Innovation/State Agency of Research MCIN/AEI/10.13039/501100011033 and by “ERDF A way of making Europe”.

References

Arce, H. G., Santiago-García, J., Jørgensen, J. K., Tafalla, M., & Bachiller, R. 2008, *ApJ*, 681, L21

Bachiller, R. 1996, *ARA&A*, 34, 111

Bachiller, R. & Pérez Gutiérrez, M. 1997, *ApJ*, 487, L93

Bachiller, R., Pérez Gutiérrez, M., Kumar, M. S. N., & Tafalla, M. 2001, *A&A*, 372, 899

Balança, C., Dayou, F., Faure, A., Wiesenfeld, L., & Feautrier, N. 2018, *MNRAS*, 479, 2692

Baskakov, O. I., Alekseev, E. A., Dyubko, S. F., & Shevrev, A. S. 1988, *Optics and Spectroscopy*, 64, 130

Ben Khalifa, M., Dagdigian, P. J., & Loreau, J. 2023, *Monthly Notices of the Royal Astronomical Society*, 523, 2577

Benedettini, M., Viti, S., Codella, C., et al. 2007, *MNRAS*, 381, 1127

Benedettini, M., Viti, S., Codella, C., et al. 2013, *MNRAS*, 436, 179

Blanco, S., López, J. C., Lesarri, A., & Alonso, J. L. 2006, *Journal of the American Chemical Society*, 128, 12111

Bocquet, R., Demaison, J., Cosléou, J., et al. 1999, *Journal of Molecular Spectroscopy*, 195, 345

Bouvier, M., Giani, L., Chahine, L., et al. 2025, *MNRAS*, 539, 2380

Burkhardt, A. M., Shingledecker, C. N., Le Gal, R., et al. 2019, *ApJ*, 881, 32

Busch, L. A., Belloche, A., Garrod, R. T., Müller, H. S. P., & Menten, K. M. 2024, *A&A*, 681, A104

Busch, L. A., Pineda, J. E., Sipilä, O., et al. 2025, *A&A*, 699, A359

Busquet, G., Fontani, F., Viti, S., et al. 2017, *A&A*, 604, A20

Ceccarelli, C., Codella, C., Balucani, N., et al. 2023, in *Astronomical Society of the Pacific Conference Series*, Vol. 534, *Protostars and Planets VII*, ed. S. Inutsuka, Y. Aikawa, T. Muto, K. Tomida, & M. Tamura, 379

Chahine, L., Ceccarelli, C., De Simone, M., et al. 2024, *MNRAS*, 534, L48

Chandra, S. & Kegel, W. H. 2000, *A&AS*, 142, 113

Chardon, J., Genty, C., Guichon, D., Sungur, N., & Theobald, J. 1974, <http://dx.doi.org/10.1051/rphysap:0197400906096100, 9>

Chen, W., Bocquet, R., Włodarczak, G., & Boucher, D. 1991, *International Journal of Infrared and Millimeter Waves*, 12, 987

Choi, M. 2001, *ApJ*, 553, 219

Choi, M. & Lee, J.-E. 2011, *Journal of Korean Astronomical Society*, 44, 201

Codella, C., Benedettini, M., Beltrán, M. T., et al. 2009, *A&A*, 507, L25

Codella, C., Ceccarelli, C., Bianchi, E., et al. 2020, *A&A*, 635, A17

Codella, C., Ceccarelli, C., Caselli, P., et al. 2017, *A&A*, 605, L3

Cortes, P. C., Pineda, J. E., Hsieh, T. H., et al. 2025, *arXiv e-prints*, arXiv:2509.21701

Dangoisse, D., Willemot, E., & Bellet, J. 1978, *Journal of Molecular Spectroscopy*, 71, 414

De Simone, M., Codella, C., Ceccarelli, C., et al. 2020, *A&A*, 640, A75

de Zafra, R. L. 1971, *ApJ*, 170, 165

DeLeon, R. L. & Muenter, J. S. 1985, *J. Chem. Phys.*, 82, 1702

Denis-Alpizar, O., Stoecklin, T., Guilloteau, S., & Dutrey, A. 2018, *Monthly Notices of the Royal Astronomical Society*, 478, 1811

Desmurs, J. F., Codella, C., Santiago-García, J., Tafalla, M., & Bachiller, R. 2009, *A&A*, 498, 753

Di Francesco, J., Myers, P. C., Wilner, D. J., Ohashi, N., & Mardones, D. 2001, *ApJ*, 562, 770

Draine, B. T. 1995, *Ap&SS*, 233, 111

Dumouchel, F., Faure, A., & Lique, F. 2010, *MNRAS*, 406, 2488

Endres, C. P., Schlemmer, S., Schilke, P., Stutzki, J., & Müller, H. S. P. 2016, *Journal of Molecular Spectroscopy*, 327, 95

Faure, A., Lique, F., & Wiesenfeld, L. 2016, *MNRAS*, 460, 2103

Fontani, F., Codella, C., Ceccarelli, C., et al. 2014, *ApJ*, 788, L43

Francis, L., van Dishoeck, E. F., Caratti o Garatti, A., et al. 2025, *A&A*, 694, A174

Gadhi, J., Lahrouni, A., Legrand, J., & Demaison, J. 1995, *Journal de Chimie Physique*, 92, 1984

Gardner, F. F., Godfrey, P. D., & Williams, D. R. 1980, *MNRAS*, 193, 713

Garrod, R. T., Jin, M., Matis, K. A., et al. 2022, *ApJS*, 259, 1

Giani, L., Ceccarelli, C., Mancini, L., et al. 2023, *MNRAS*, 526, 4535

Gieser, C., Caselli, P., Segura-Cox, D. M., et al. 2025, *arXiv e-prints*, arXiv:2507.16303

Gieser, C., Pineda, J. E., Segura-Cox, D. M., et al. 2024, *A&A*, 692, A55

Goldsmith, P. F. & Langer, W. D. 1999, *ApJ*, 517, 209

Gusdorf, A., Cabrit, S., Flower, D. R., & Pineau Des Forets, G. 2008, *A&A*, 482, 809

Herbst, E. & van Dishoeck, E. F. 2009, *ARA&A*, 47, 427

Herczeg, G. J., Karska, A., Bruderer, S., et al. 2012, *A&A*, 540, A84

Hily-Blant, P., Walmsley, M., Pineau Des Forets, G., & Flower, D. 2010, *A&A*, 513, A41

Hirota, E., Sugisaki, R., Nielsen, C. J., & Sørensen, G. O. 1974, *Journal of Molecular Spectroscopy*, 49, 251

Jiménez-Serra, I., Caselli, P., Martín-Pintado, J., & Hartquist, T. W. 2008, *A&A*, 482, 549

Jørgensen, J. K., Bourke, T. L., Myers, P. C., et al. 2007, *ApJ*, 659, 479

Kryvda, A. V., Gerasimov, V. G., Dyubko, S. F., Alekseev, E. A., & Motienko, R. A. 2009, *Journal of Molecular Spectroscopy*, 254, 28

Kukolich, S. G. & Nelson, A. C. 1971, *Chemical Physics Letters*, 11, 383

Kurland, R. J. & Bright Wilson, Jr., E. 1957, *J. Chem. Phys.*, 27, 585

Kwon, W., Fernández-López, M., Stephens, I. W., & Looney, L. W. 2015, *ApJ*, 814, 43

Lefloch, B., Ceccarelli, C., Codella, C., et al. 2017, *MNRAS*, 469, L73

Lenzini, P., Gail, H.-P., & Henning, T. 1995, *ApJ*, 447, 848

López-Sepulcre, A., Codella, C., Ceccarelli, C., Podio, L., & Robuschi, J. 2024, *A&A*, 692, A120

Mallinson, P. D. & de Zafra, R. L. 1978, *Molecular Physics*, 36, 827

Maret, S., Hily-Blant, P., Pety, J., Bardeau, S., & Reynier, E. 2011, *A&A*, 526, A47

McKee, C. F. & Hollenbach, D. J. 1980, *ARA&A*, 18, 219

Mendoza, E., Lefloch, B., Ceccarelli, C., et al. 2018, *MNRAS*, 475, 5501

Mendoza, E., Lefloch, B., López-Sepulcre, A., et al. 2014, *MNRAS*, 445, 151

Miranzo-Pastor, J. J., Fuente, A., Navarro-Almaida, D., et al. 2025, *A&A*, 700, A251

Moskienko, E. M. & Dyubko, S. F. 1991, *Radiophysics and Quantum Electronics*, 34, 181

Motienko, R. A. & Margulès, L. 2025, *A&A*, 699, A348

Müller, H. S. P., Brown, L. R., Drouin, B. J., et al. 2015, *Journal of Molecular Spectroscopy*, 312, 22

Pearson, J. C., Müller, H. S. P., Pickett, H. M., Cohen, E. A., & Drouin, B. J. 2010, *J. Quant. Spectr. Rad. Transf.*, 111, 1614

Pearson, J. C., Yu, S., & Drouin, B. J. 2012, *Journal of Molecular Spectroscopy*, 280, 119

Pineda, J. E., Sipilä, O., Segura-Cox, D. M., et al. 2024, *A&A*, 686, A162

Podio, L., Ceccarelli, C., Codella, C., et al. 2024, *A&A*, 688, L22

Podio, L., Codella, C., Gueth, F., et al. 2016, *A&A*, 593, L4

Podio, L., Tabone, B., Codella, C., et al. 2021, *A&A*, 648, A45

Rabli, D. & Flower, D. R. 2010, *MNRAS*, 406, 95

Sahnoun, E., Wiesenfeld, L., Hammami, K., & Jaidane, N. 2018, *Journal of Physical Chemistry A*, 122, 3004

Sakai, N., Ceccarelli, C., Bottinelli, S., Sakai, T., & Yamamoto, S. 2012, *ApJ*, 754, 70

Schöier, F. L., van der Tak, F. F. S., van Dishoeck, E. F., & Black, J. H. 2005, *A&A*, 432, 369

Segura-Cox, D. M., Looney, L. W., Tobin, J. J., et al. 2018, *ApJ*, 866, 161

Smirnov, I. A., Alekseev, E. A., Ilyushin, V. V., et al. 2014, *Journal of Molecular Spectroscopy*, 295, 44

Spezzano, S., Caselli, P., Sipilä, O., & Bizzocchi, L. 2022, *A&A*, 664, L2

Stephens, I. W., Dunham, M. M., Myers, P. C., et al. 2018, *ApJS*, 237, 22

Sugimura, M., Yamaguchi, T., Sakai, T., et al. 2011, *PASJ*, 63, 459

Taniguchi, K., Herbst, E., Caselli, P., et al. 2019, *ApJ*, 881, 57

Thorwirth, S., Müller, H. S. P., & Winnewisser, G. 2000, *Journal of Molecular Spectroscopy*, 204, 133

Tobin, J. J., Looney, L. W., Li, Z.-Y., et al. 2016, *ApJ*, 818, 73

Tucker, K. D. & Tomasevich, G. R. 1973, *Journal of Molecular Spectroscopy*, 48, 475

Valdivia-Mena, M. T., Pineda, J. E., Caselli, P., et al. 2024, A&A, 687, A71
 van Dishoeck, E. F., Tychoniec, Ł., Rocha, W. R. M., et al. 2025, arXiv e-prints, arXiv:2505.08002
 Vorob'eva, E. M. & Dyubko, S. F. 1994, Radiophysics and Quantum Electronics, 37, 155
 Wiesenfeld, L. & Faure, A. 2013, MNRAS, 432, 2573
 Xu, L.-H., Fisher, J., Lees, R. M., et al. 2008, Journal of Molecular Spectroscopy, 251, 305
 Yamada, K. M. T., Moravec, A., & Winnewisser, G. 1995, Zeitschrift Naturforschung Teil A, 50, 1179
 Yang, B., Stancil, P. C., Balakrishnan, N., & Forrey, R. C. 2010, ApJ, 718, 1062
 Yıldız, U., Goldsmith, P., Pineda, J., & Langer, W. 2015, in American Astronomical Society Meeting Abstracts, Vol. 225, American Astronomical Society Meeting Abstracts #225, 451.09
 Zucker, C., Speagle, J. S., Schlaflay, E. F., et al. 2019, ApJ, 879, 125

¹ Max-Planck-Institut für extraterrestrische Physik, Gießenbachstraße 1, 85748 Garching bei München, Germany

² Department of Physics and Astronomy, University of Rochester, Rochester, NY 14627, USA

³ Max-Planck-Institut für Astronomie, Königstuhl 17, D-69117 Heidelberg, Germany

⁴ Taiwan Astronomical Research Alliance (TARA), Taiwan

⁵ Institute of Astronomy and Astrophysics, Academia Sinica, P.O. Box 23-141, Taipei 106, Taiwan

⁶ European Southern Observatory, Karl-Schwarzschild-Straße 2, 85748 Garching, Germany

⁷ Institute de Radioastronomie Millimétrique (IRAM), 300 rue de la Piscine, F-38406, Saint-Martin d'Hères, France

⁸ Zentrum für Astronomie der Universität Heidelberg, Institut für Theoretische Astrophysik, Albert-Ueberle-Str. 2, 69120 Heidelberg, Germany

⁹ Centro de Astrobiología (CAB), CSIC-INTA, Ctra. de Ajalvir Km. 4, 28850, Torrejón de Ardoz, Madrid, Spain

¹⁰ Joint ALMA Observatory, Alonso de Córdova 3107, Vitacura, Santiago, Chile

¹¹ National Radio Astronomy Observatory, 520 Edgemont Road, Charlottesville, VA 22903, USA

¹² Department of Astronomy, University of Illinois, 1002 W Green St., Urbana, IL 61801, USA

¹³ Department of Earth, Environment and Physics, Worcester State University, Worcester, MA 01602, USA

¹⁴ Observatorio Astronómico Nacional (IGN), Alfonso XII 3, E-28014, Madrid, Spain

¹⁵ Laboratoire d'Astrophysique de Bordeaux, Université de Bordeaux, CNRS, B18N, Allée Geoffroy Saint-Hilaire, F-33615 Pessac, France

¹⁶ Department of Earth Science Education, Seoul National University, 1 Gwanak-ro, Gwanak-gu, Seoul 08826, Republic of Korea

¹⁷ SNU Astronomy Research Center, Seoul National University, 1 Gwanak-ro, Gwanak-gu, Seoul 08826, Republic of Korea

Appendix A: Additional tables and figures

Figure A.1 shows example spectra towards positions R1 and B1 (Fig. 1) for selected molecules. Vertical lines indicate the integration limits used for Figs. 1, 2, and A.3. Figure A.2 shows channel maps towards the IRAS 4B Class 0 binary of SiO and CO using PRODIGE data and CH_3OH and C^{34}S using ALPPS data. Intensities were integrated from -33 to 47 km s^{-1} in 10 km s^{-1} intervals for SiO and CO and from 3 to 11 km s^{-1} in 2 km s^{-1} intervals for CH_3OH and C^{34}S . The ALPPS data at $3\text{--}4\times$ higher angular resolution reveal the highly structured outflow morphology. Figure A.3 shows integrated intensity maps of red- and blueshifted emission from various organic molecules using the PRODIGE data. The derived population diagrams are shown in Fig. A.4.

Table A.1 summarises spectroscopic properties of molecular transitions used for the various maps in this work. Table A.2 shows the results of the LTE spectral-line analyses towards positions IRAS 4B1-B1 and IRAS 4B1-R1 in the outflow, using the radiative transfer code Weeds (Maret et al. 2011) and population diagrams (Goldsmith & Langer 1999). Column densities derived towards the L1157-B1 outflow shock spot are provided as well. Table A.3 provides references for the spectroscopic information for the analysed molecules.

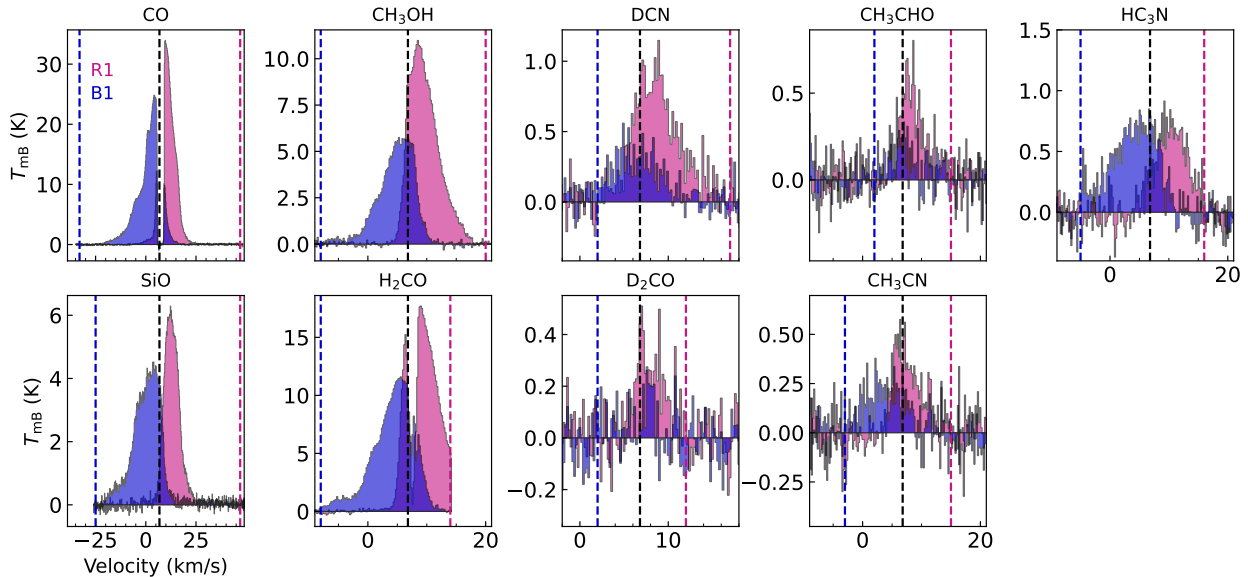


Fig. A.1. Average spectra of selected molecules extracted from a $1''$ aperture towards positions R1 and B1 (see Fig. 1). The black dashed line indicates the systemic velocity of 6.8 km s^{-1} , while red and blue dashed lines indicate the outer integration limits for the respective molecule used in Figs. 1, 2, and A.3. Despite the narrow band not covering all H_2CO emission, we used it for the H_2CO map as it shows more structure.

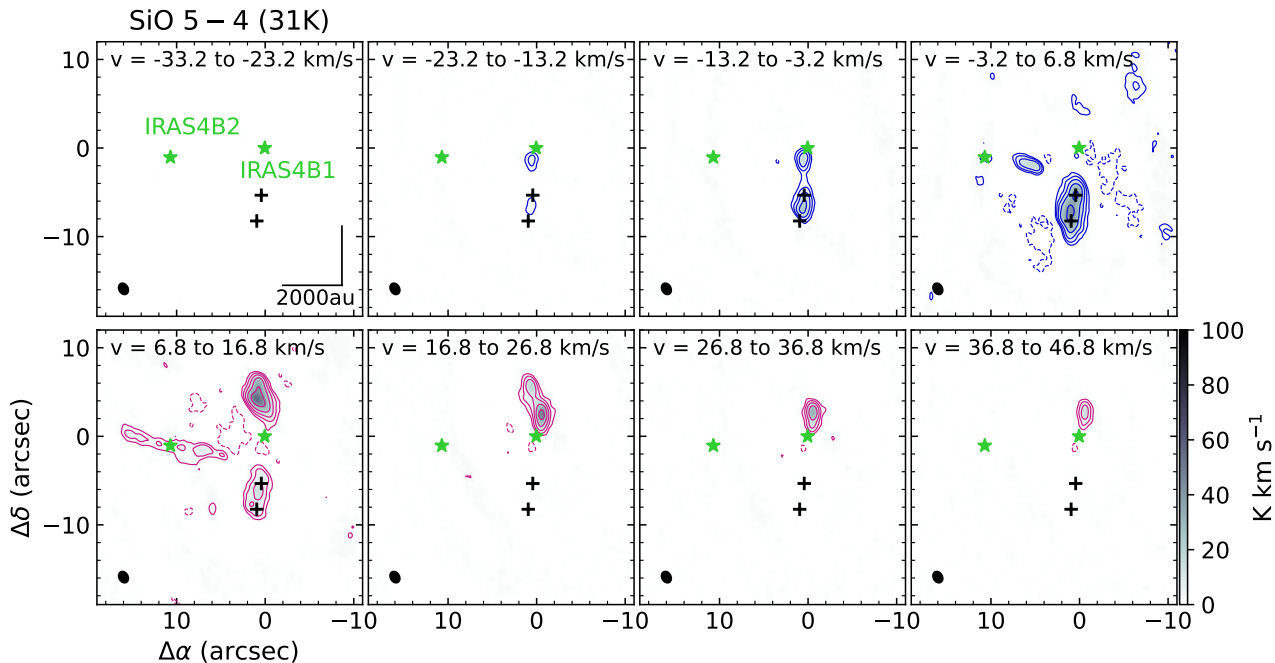
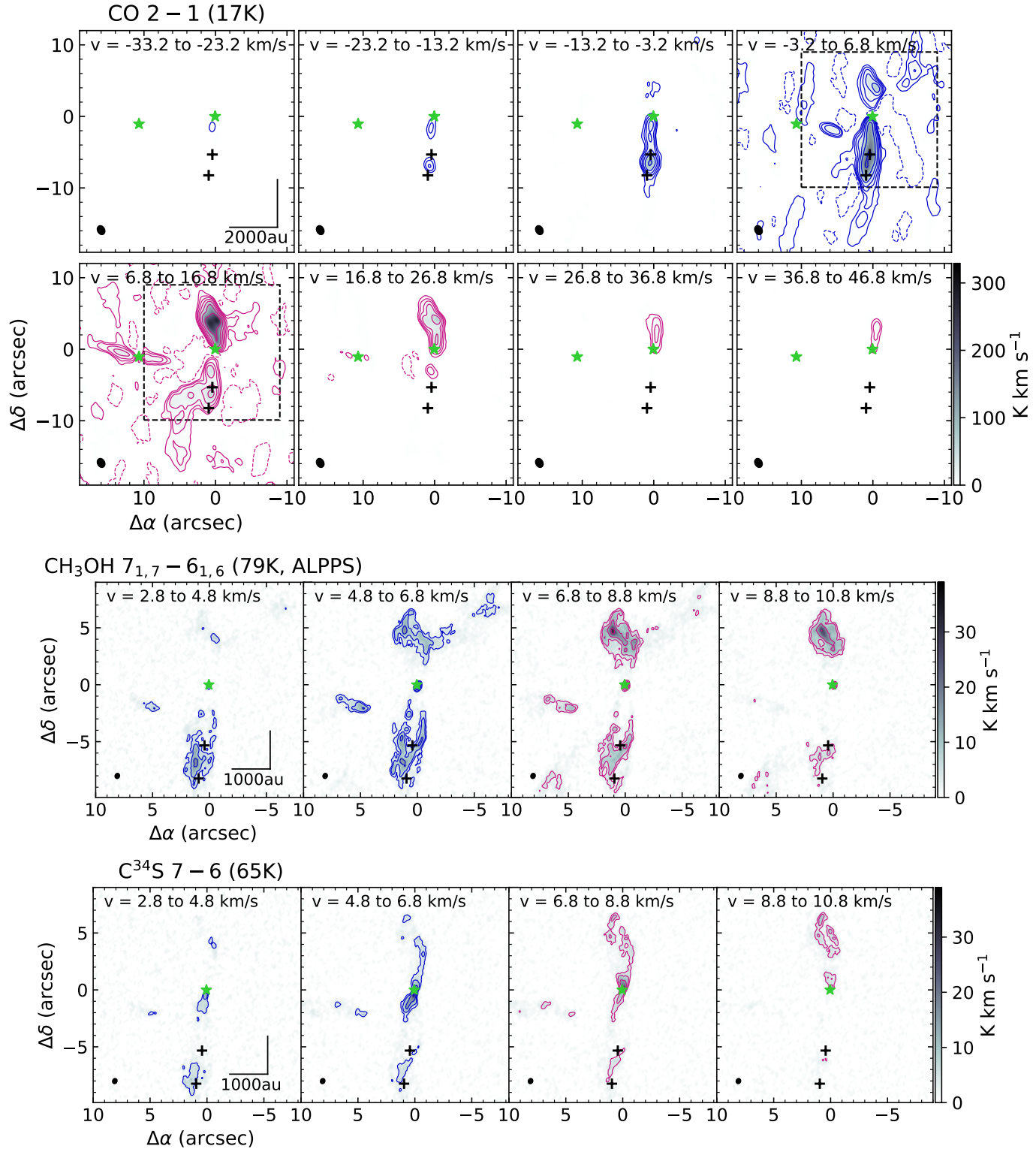


Fig. A.2. Integrated intensity maps for SiO and CO (PRODIGE) towards IRAS 4B1 and IRAS 4B2 (green stars) and for CH_3OH and C^{34}S (ALPPS, next page) zoomed in (cf. black dashed rectangle in CO panels) on IRAS 4B1. Intensities were integrated over intervals of 10 km s^{-1} (SiO and CO) and 2 km s^{-1} (CH_3OH and C^{34}S). Contour levels are at -10σ , 10σ and then increase by a factor 2, where $\sigma = 0.24 \text{ K km s}^{-1}$ (SiO), 0.27 K km s^{-1} (CO), and 0.34 K km s^{-1} (CH_3OH and C^{34}S). Black crosses mark H_2 knots (Choi & Lee 2011). The HPBWs are shown in the bottom left.

**Fig. A.2.** continued.

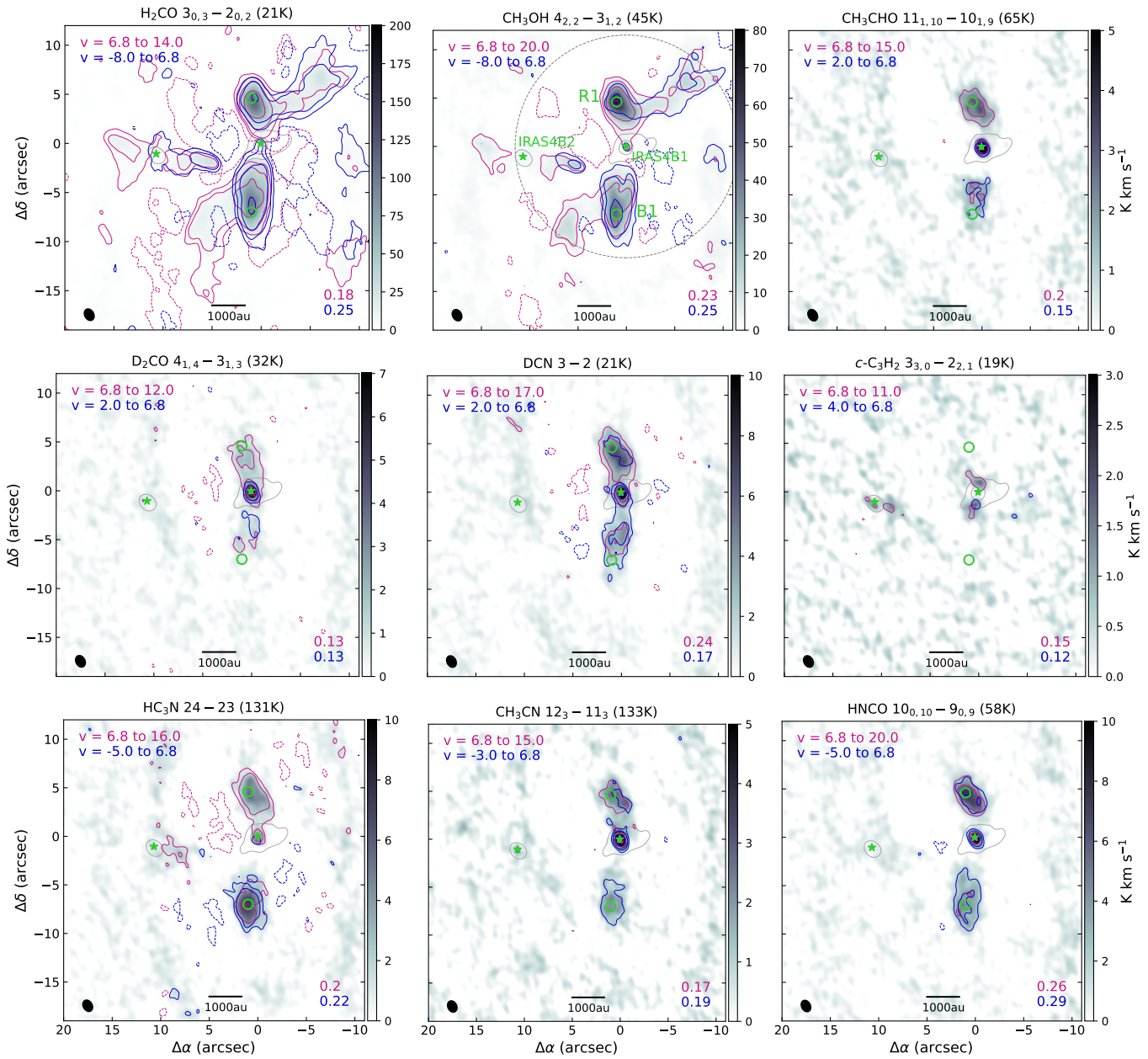


Fig. A.3. Integrated intensity maps towards IRAS 4B1 and 4B2 (green stars) for the molecular transitions that are written on top with their respective upper-level energy. Contours are at -5σ , 5σ , 10σ , and then increase by a factor 3 for all but SiO, CO, H₂CO, and CH₃OH, for which contours start at -10σ and 10σ . The noise levels, σ , are measured in the respective maps and are written in the bottom right. Velocity (in km s^{-1}) ranges for integration are indicated in the top left. The grey scale shows the sum of the red- and blueshifted maps. The HPBW is shown in the bottom left. The dashed grey circle indicates the primary beam ($\sim 23''$). Positions R1 and B1 (green circles) are selected for further spectral-line analysis.

Table A.1. Molecular transitions used in this work for integrated intensity and temperature maps.

Molecule	Transition	Frequency (MHz)	E_u^a (K)	A_u^b (s^{-1})	g_u^c	$n_{\text{crit},T}^d$ (cm^{-3})	Survey ^e	Refs. ^f
CO	2 – 1	230538.000	16.6	6.9(–7)	5	1(4)	P	Yang et al. (2010), Balança et al. (2018)
SiO	5 – 4	217104.919	31.3	5.2(–4)	11	3(6)	P	Denis-Alpizar et al. (2018)*
C ³⁴ S	7 – 6	337396.459	64.8	7.6(–4)	15	9(6)	A	Chandra & Kegel (2000)
c-C ₃ H ₂	3 _{3,0} – 2 _{2,1}	216278.756	19.5	2.6(–4)	21	5(7)	P	Wiesenfeld & Faure (2013)
H ₂ CO	3 _{0,3} – 2 _{0,2}	218222.192	21.0	2.8(–4)	7	3(6)	P	Dumouchel et al. (2010)*
DCN	3 – 2	217238.612	20.9	4.6(–4)	9	4(7)	P	Wiesenfeld & Faure (2013)*
D ₂ CO	4 _{1,4} – 3 _{1,3}	221191.661	32.0	2.8(–4)	9	4(6)	P	Rabli & Flower (2010)
CH ₃ OH	5 _{1,4} – 4 _{2,2}	216945.521	55.9	1.2(–5)	44	7(6)	P	
	4 _{2,2} – 3 _{1,2}	218440.063	45.5	4.7(–5)	36	8(7)	P	
	10 _{2,9} – 9 _{3,6}	231281.110	165.3	1.8(–5)	84	3(7)	P	
	7 _{1,7} – 6 _{1,6}	335582.017	79.0	1.6(–4)	60	2(6)	A	
	12 _{1,11} – 12 _{0,12}	336865.149	197.1	4.1(–4)	100	9(7)	A	
CH ₃ CHO	11 _{1,10} – 10 _{1,9}	216581.933	64.9	3.5(–4)	23	–	P	
HC ₃ N	24 – 23	218324.723	131.0	8.3(–4)	49	2(7)	P	Faure et al. (2016)
	37 – 36	336520.084	306.9	3.1(–3)	75	1(7)	A	
CH ₃ CN	12 ₃ – 11 ₃	220707.753	133.2	6.0(–6)	50	2(5)	P	Ben Khalifa et al. (2023)
HNCO	10 _{1,10} – 9 _{1,9}	219798.274	58.0	1.5(–4)	21	2(6)	P	Sahnoun et al. (2018)

Notes. Spectroscopic information are taken from the Leiden Atomic and Molecular Database (LAMDA; Schöier et al. 2005).

^(a)Upper-level energy. ^(b)Einstein A coefficient, where $x(y) = x \times 10^y$. ^(c)Statistical weight. ^(d)Critical density estimate, $n_{\text{crit},T} = A_u/C_u$, for $T = 100\text{ K}$. The collisional rate coefficients are taken from the references in column nine. ^(e)Survey designation: P = PRODIGE, A = ALPPS.

^(f)References for collisional rate coefficients. ^(g)Collisional rate coefficients are for the transition of the main isotopologues.

Table A.2. Weeds parameters and results of the population-diagram analysis. References to spectroscopic information used for the analysis are given in Table A.3.

Molecule ^a	P	$T_{\text{rot},W}^b$ (K)	$T_{\text{rot},\text{PD}}^c$ (K)	$N_{\text{tot},W}^d$ (cm^{-2})	$N_{\text{tot},\text{PD}}^e$ (cm^{-2})	Δv^f (km s^{-1})	v_{off}^g (km s^{-1})	$N_{\text{L1157-B1}}^h$ (cm^{-2})
D ₂ CO	R1	60	51 ± 15	2.8(13)	$(2.9 \pm 1.1)(13)$	4.5	2.0	
	B1	60	58 ± 41	1.6(13)	$(2.1 \pm 1.9)(13)$	4.5	–0.5	
CH ₃ OH	R1	80	76 ± 9	5.0(15)	$(5.1 \pm 2.3)(15)$	5.0	2.5	$(1.3 \pm 0.3)(16)$
	B1	80	80	3.5(15)	$(4.0 \pm 1.0)(15)$	6.5	–1.5	
CH ₂ DOH	R1	100	100	4.5(14)	$(6.5 \pm 1.8)(14)$	3.5	1.5	$(2.2 \pm 0.7)(14)$
	B1	100	100	3.0(14)	$(3.6 \pm 3.6)(14)$	4.5	–1.5	
CH ₃ CHO	R1	60	58 ± 3	1.5(14)	$(2.0 \pm 0.2)(14)$	4.5	2.5	$(7.0 \pm 3.0)(13)$
	B1	60	64 ± 17	8.0(13)	$(1.1 \pm 0.6)(14)$	4.5	–1.5	
HC ₃ N	R1	75	74 ± 1	2.0(13)	$(2.2 \pm 0.1)(13)$	6.0	3.0	3.4(13)
	B1	80	74 ± 3	2.8(13)	$(3.6 \pm 0.5)(13)$	7.0	–2.5	
CH ₃ CN	R1	90	91 ± 11	1.9(13)	$(2.2 \pm 0.4)(13)$	5.5	2.5	1.0(13)
	B1	90	108 ± 6	1.5(13)	$(2.1 \pm 0.2)(13)$	5.5	–1.5	
NH ₂ CHO	R1	50		$< 1.5(13)$		5.0	2.5	8.0(12)
	B1	50		$< 1.5(13)$		5.0	–2.5	

Notes. Values in parentheses show the decimal power, where $x(z) = x \times 10^z$ or $(x \pm y)(z) = (x \pm y) \times 10^z$.

^(a) Detected molecule and vibrational state used to derive population diagrams. ^(b) Rotational temperature used for the Weeds model. ^(c) Rotational temperature derived from the population diagram. When a value has no error, it was fixed. ^(d) Column density used for the Weeds model. An upper limit on $N_{\text{tot},W}$ indicates that the molecule is not detected. ^(e) Column density derived from the population diagram. ^(f) FWHM of the spectral lines. ^(g) Offset from $v_{\text{sys}} = 6.8\text{ km s}^{-1}$. ^(h) Column densities derived from interferometric observations towards L1157-B1: CH₃OH and CH₃CHO (Codella et al. 2020), HC₃N (Benedettini et al. 2007), CH₃CN (Codella et al. 2009), CH₂DOH (Fontani et al. 2014), and NH₂CHO (Codella et al. 2017).

Table A.3. Spectroscopic references for the analysed molecules in Table A.2.

Molecule	DB ^a	References
D ₂ CO	CDMS	Tucker & Tomasevich (1973), Chardon et al. (1974), Dangoisse et al. (1978), Baskakov et al. (1988), Bocquet et al. (1999)
CH ₃ OH	CDMS	Xu et al. (2008)
CH ₂ DOH	JPL	Pearson et al. (2012)
CH ₃ CHO	LSD	Smirnov et al. (2014)
HC ₃ N	CDMS	de Zafra (1971), Mallinson & de Zafra (1978), DeLeon & Muenter (1985), Chen et al. (1991), Yamada et al. (1995), Thorwirth et al. (2000)
CH ₃ CN	CDMS	Müller et al. (2015), Gadhi et al. (1995)
NH ₂ CHO	CDMS	Kurland & Bright Wilson (1957), Kukolich & Nelson (1971), Hirota et al. (1974), Gardner et al. (1980), Moskienko & Dyubko (1991), Vorob'eva & Dyubko (1994), Blanco et al. (2006), Kryvda et al. (2009)

Notes. ^(a)Database (DB): Cologne database for molecular spectroscopy (CDMS; Endres et al. 2016), Lille spectroscopic database (LSD; Motiyenko & Margulès 2025), Jet Propulsion Laboratory (JPL) catalogue (Pearson et al. 2010).

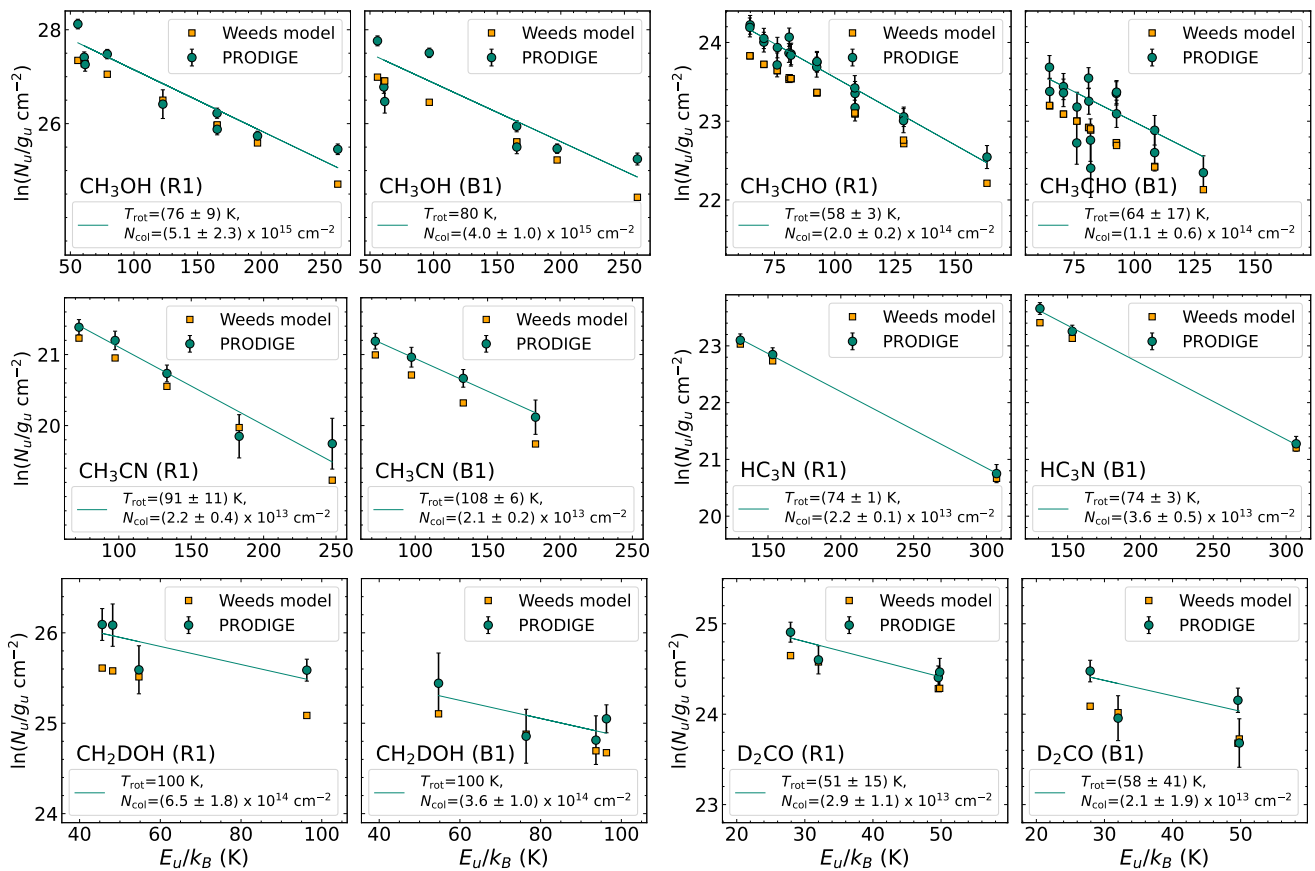


Fig. A.4. Population diagrams towards positions R1 and B1 (see Fig. A.3). The results of the linear fit to the observed data points (teal circles) are shown in the bottom. The observed data were corrected for contaminating emission, and both observed and modelled data (orange squares) are corrected for optical depth (for details see Busch et al. 2025).